



EXPERIMENTAL INVESTIGATION OF THE EFFECT OF STRAIN RATE ON THE CRUSHING STRENGTH OF A CELLULAR CONCRETE

Burak AKYOL¹, Mustafa GÜDEN^{2*}, Alper TAŞDEMİRÇİ³,
Subhan NAMAZOV⁴

^{1,2*,3}Dynamic Testing and Modeling Laboratory and Department of Mechanical Engineering, Izmir Institute of Technology, Izmir, Turkey

⁴Vice-rector for science and innovation of Azerbaijan Technical University, Baku, Azerbaijan

E-mail: burakakyol@iyte.edu.tr¹, mustafaguden@iyte.edu.tr^{2*}, alpertasdemirci@iyte.edu.tr³,
subhan_namazov@daad-alumni.de⁴

Abstract: The strain rate dependent compressive strength of an autoclaved aerated concrete (AAC) having a density of 600 kg m^{-3} was experimentally investigated between quasi-static and high strain rates (2×10^{-3} – 4150 s^{-1}) through quasi-static and dynamic compression, confined compression and indentation tests. High strain rate equilibrium and direct impact non-equilibrium compression tests in conjunction with the high strain rate confined compression and indentation tests were conducted in a compression Split Hopkinson Pressure Bar. The experimental results showed two different regions of the compressive strength-dependency on the strain rate: a low-strain rate-dependent region from quasi-static to $\sim 18 \text{ s}^{-1}$ and a high-strain rate-dependent region from $\sim 18 \text{ s}^{-1}$ to $\sim 1000 \text{ s}^{-1}$. The switch of the failure mode from the single axial cracking at quasi-static strain rates to the extensive axial and circumferential cracking at increasing strain rates was ascribed to both the axial and radial inertia. The dynamic increased factor (DIF=dynamic strength/static strength) showed an abrupt increase after $\sim 18 \text{ s}^{-1}$ as similar with the compressive strength. The mean confined and indentation strength values also increased as the velocity increased, while the mean confined compression strength values were shown to be comparable with the dynamic compressive strength values. The inertia and strain rate contributions to the enhancement of DIF until about 1000 s^{-1} were predicted by taking the quasi-static indentation strength as the full confinement strength.

Keywords: Autoclaved aerated concrete; Split Hopkinson Pressure Bar; direct impact; compressive strength; indentation; confinement; inertia

Introduction. Autoclaved aerated concrete (AAC) is a light-weight cellular material with relatively high compressive strength, low thermal conductivity, high sound absorptivity, non-flammability and high durability [1]. AAC is processed by foaming a ceramic slurry of sand, lime, cement and water in the presence of a foaming agent i.e. aluminum powder and has become one of the most widely used building materials [2]. It is applied mainly as the heat and sound insulation material and also as the structural element. Most of the previous studies on the determination of the mechanical properties of AAC have been so far at quasi-static strain rates; examples can be found in [1, 3-8]. However, the dynamic loading of the AAC-based structures is quite possible under extreme loading conditions such as earthquakes, explosions and projectile impacts. But, there have been few experimental and numerical studies, based on the authors' knowledge, on the dynamic loading behavior of AAC in the literature as will be shortly reviewed here. The shock stress response of an AAC (500 kg m^{-3}) was previously investigated [9]. Radial and spalling cracks were detected and the source-distance was shown the main factor affecting the number of cracks formed. The quasi-static and dynamic compression mechanical behavior of an AAC sample (550 kg m^{-3}) were determined until about 104 s^{-1} [10]. In the confined compression tests, the samples were completely densified with a continuous load-displacement behavior. The dynamic compressive strength increased by 45% of the quasi-static strength at 515 s^{-1} and the damage formed earlier in dynamically tested samples. Dry and water-saturated AAC samples were tested between 1.4×10^2 and $1 \times 10^3 \text{ s}^{-1}$ [11]. The failure

strength showed a positive strain rate sensitivity from quasi-static up to a critical strain rate; thereafter, the samples were pulverized near the plane of impact.

The strength enhancement in brittle rock-like materials is generally presented by the dynamic increase factor (DIF=dynamic fracture strength/static fracture strength). The DIF of concrete was reported to vary between 1 and 2.5 from static to dynamic strain rates with a sudden increase after about 100 s^{-1} [12]. The compressive strength of limestone was shown to increase slowly with strain rate up to 10^3 s^{-1} ; thereafter, increased sharply, approaching the shock fracture strength [13]. An “s-type” dependence of the fracture strength of brittle materials on strain rate was proposed as schematically shown in Figure 1 [14].

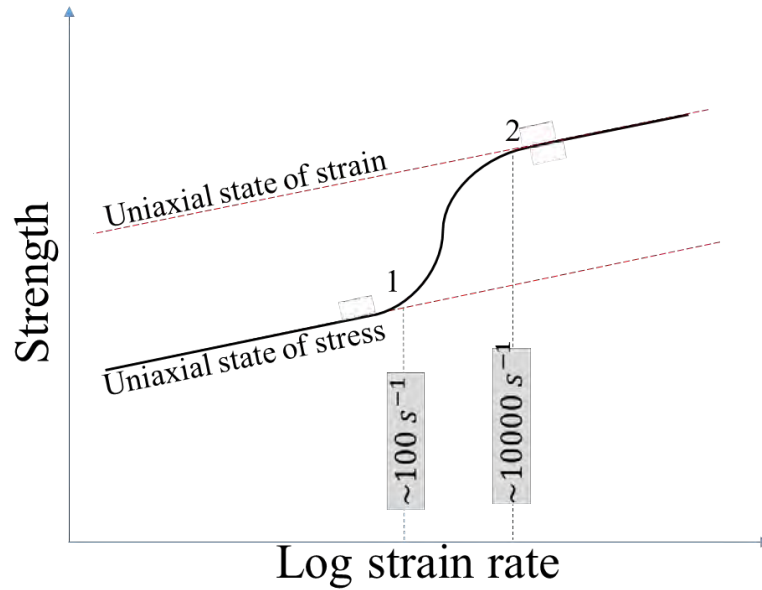


Figure 1. The schematic of the variation of the strength of brittle materials with strain rate, adapted from reference [14]

On this “s-type” curve, there are two turning points: (1) from a low-strain rate-dependent strength to a high-strain rate-dependent strength region and (2) from a high-strain rate-dependent strength to again a low-strain rate-dependent strength region. The first and second turning points were broadly proposed as 10^2 and 10^4 s^{-1} for concrete, respectively [15]. The low-strain rate-dependent strength region was ascribed to the strain-rate dependent growth of tensile micro cracks (thermally activated mechanism) and viscous behavior of bulk material between cracks (Stefan effect) [16-18]. Since the energy needed for crack opening is much higher than the energy needed for crack growth at quasi-static strain rates, few cracks grow under static loading through the weakest path along axial direction. There is however less time for both crack opening and growth at increasing strain rates, causing an increase in the dynamic strength and number of micro cracks formed. [17-19]. The water content increased the strain rate sensitivity of concrete under tension [20] and compression [21] and altered the compression failure mode [21]. The increased strain rate sensitivity of wet concrete was ascribed to viscous mechanism in several references [21-23]. At increasing strain rates, an elastically deforming structure cannot expand in the transverse direction (Poisson’s expansion) due to the radial inertia restraint. The radial inertia imposes a confinement stress on the deforming structure, transforming the deformation from a uniaxial state of stress to a uniaxial state of strain. The increase in the strength of concrete after a critical velocity was ascribed to the development of a uniaxial state of strain [13, 24-27]. Modelling SHPB tests on concrete using a pressure dependent strength model showed that the stress triaxiality was near 1D state of stress at 47 s^{-1} , while it reached 1D state of strain at $\sim 795 \text{ s}^{-1}$ [28]. Above this critical strain rate, the sample deformation was completely 1D state of strain. The explained pseudo strain rate effect occurs when the compressive strength of the tested sample is hydrostatic pressure sensitive and lateral confinement is developed

on the sample. A current concrete model has adapted a cut-off value of 2.94 to cap DIF above 300s^{-1} [28]. But, it is not clear whether or not this capping occurs in or after the high-strain rate-dependent strength region. The inertia corrected stress of a cylindrical sample under compression was given by Davies and Hunter in 1963 [29]

$$\sigma_c = \sigma_A + \left[\left(\frac{h^2}{3} \right) + \nu^2 \left(\frac{d^2}{8} \right) \right] \rho \ddot{\epsilon}(t) \quad (1)$$

where σ_A is the average stress, h and d are sequentially the height and diameter of a cylindrical sample and ρ and ν are the density and Poisson's ratio of the test material, respectively. The second and third terms in Eqn. 1 are the axial and radial inertia stress term, respectively. As noted in the above equation, confining the sample during deformation eliminates the stress rise due to radial inertia.

The main motivation for the present study is the lack of a comprehensive experimental study on the strain rate dependent compressive strength of AAC as stated earlier. Therefore, the strain rate sensitive compressive strength of an AAC was investigated experimentally in order to determine the effect of strain rate on the crushing behavior. Various test methods including quasi-static and dynamic compression, drop-weight compression and direct impact tests were applied. The quasi-static compression tests were performed at the velocities between 5×10^{-5} to $5 \times 10^{-3} \text{ m s}^{-1}$, corresponding to the strain rates of 2×10^{-3} and $2 \times 10^{-1} \text{ s}^{-1}$. The low-velocity impact tests were performed in a drop-weight set-up at a velocity of $\sim 1 \text{ m s}^{-1}$, corresponding to $\sim 35 \text{ s}^{-1}$. The dynamic compression tests were performed in a compression type Split Hopkinson Pressure Bar (SHPB) at the velocity of 8 m s^{-1} , corresponding to $\sim 185 \text{ s}^{-1}$ and the direct impact tests between 10 and 108 m s^{-1} , corresponding to ~ 385 and $\sim 4150 \text{ s}^{-1}$. The direct impact tests were non-equilibrium tests and analyzed differently from the compression SHPB tests.

Materials and testing

Sample preparation

AAC blocks and plates (600 kg m^{-3}) were provided by one of the biggest AAC producers in Turkey, AKG Gaz Beton. The quasi-static and dynamic compression test samples, $\sim 19.4 \text{ mm}$ in diameter and 26 mm in length, were cored-drilled from 26 mm -thick AAC plates using a core-drilling machine. Figures 2(a-c) show the pictures of a 26 mm -thick core-drilled AAC plate, fracture surface of an AAC sample and the core-drilled compression test samples, respectively. As seen in Figure 2(b), the tested AAC had a typical cellular structure, composing of cells and cell walls and edges. The cell sizes were measured using an image analyzer on the pictures of the fracture surfaces of few samples. At least 120 cells were counted and the results were averaged. The average cell size was determined 0.5 mm using above method. No coolant was used in the core-drilling and the surfaces of cylindrical compression test samples were cleaned after drilling by applying pressurized air. The indentation tests were directly performed on the flat surfaces of AAC blocks. Before testing, the core-drilled compression test samples and the blocks for the indentation tests were kept in an oven at 70°C for 24 h (standard procedure).

The same sample sizes were used in the quasi-static, SHPB and direct impact compression tests. The maximum diameter of test samples was limited by the diameter of the bars of the used SHPB (19.45 mm). The sample size can affect the critical strain rate for the inertia dominated deformation. It may also alter the strength since the strength of brittle materials is volume dependent (the probability of the presence of larger microstructural defects). Larger samples exhibit lower strength. On the other hand, smaller samples may not represent the homogeneous mechanical properties, which requires at least 8-10 cells in one dimension [30, 31]. The tested samples in the present study contained much more cells (0.5 mm cell size) than the critical number cells.

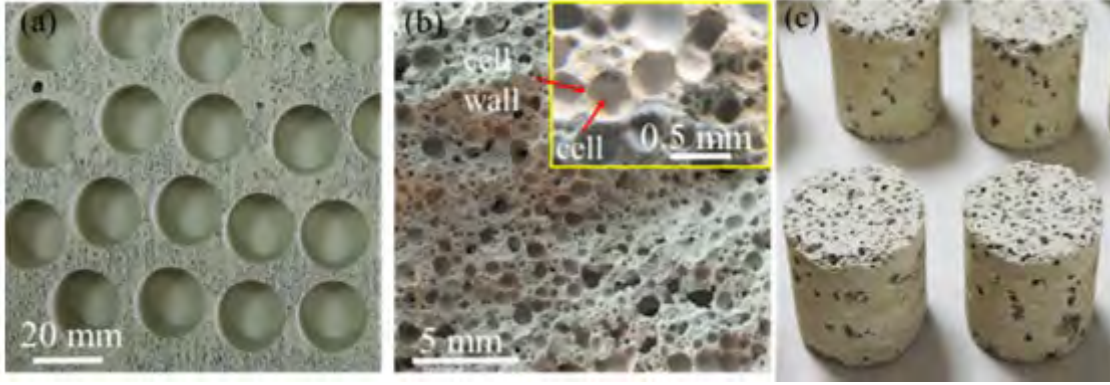


Figure 2. The pictures of (a) a core-drilled 26 mm-thick plate, (b) the fracture surface of a AAC sample (showing the typical foam cellular structure) and (c) the compression test samples after core-drilling

Unconfined quasi-static and high strain rate compression tests

Quasi-static compression tests were performed in a Shimadzu AG-X Universal Test machine in accord with ASTM C39/C 39M-03 “Standard Test Method for Compressive Strength of Cylindrical Concrete Specimens” [32]. Three different cross-head speeds were used in the quasi-static compression tests; 5×10^{-5} , 5×10^{-4} , and 5×10^{-3} m s⁻¹, corresponding to the strain rates of $\sim 2 \times 10^{-3}$, $\sim 2 \times 10^{-2}$ and $\sim 2 \times 10^{-1}$ s⁻¹, respectively. The strain was calculated as the nominal strain (elongation divided by initial length) and determined both from the machine stroke and the video extensometer synchronized to the test machine. In all compression tests, an axis-aligned pin-ball upper compression test platen was used and the sample deformation was recorded by using a video camera.

The low velocity compression tests were performed in a FRACTOVIS drop-weight tester using a 90 kN-90 mm-diameter flat-end striker. A photocell-circuit was used to measure the striker velocity at 1000 kHz. The initial striker velocity was varied between 1.05 and 1.1 m s⁻¹, corresponding to a strain rate between 34 and 38 s⁻¹. The striker velocity decreased only ~ 0.1 m s⁻¹ until the fracture. The energy absorbed by the AAC samples was calculated ~ 0.4 J by taking the fracture strength 7.34 MPa and the fracture strain 0.015. The striker energy was therefore far greater than the energy absorbed by the sample by taking into account an applied weight of 6.42 kg and the mass of the striker itself. The deformation was further recorded by a Fastcam Photron high speed camera at 20000 fps.

The SHPB apparatus used in the high strain rate tests consisted of 19.45 mm diameter Inconel 718 incident (3110 mm), transmitter (2050 mm) and striker (500 mm) bar. The elastic modulus and density of bars were 204 GPa and 8394 kg m⁻³, respectively. The schematic of the used SHPB test system is shown in Figure 3(a). The strains on the bars were measured by a full Wheatstone-bridge configuration of 350 Ω foil strain gauges. The velocity of the striker bar was measured using laser-velocity gates mounted at the exit of the gas barrel and also from the Fastcam Photron high speed camera records of the striker bar. Based on the stress equilibrium, the strain (ϵ_s), stress (σ_s) and strain rate ($\dot{\epsilon}_s$) of the sample are [33]

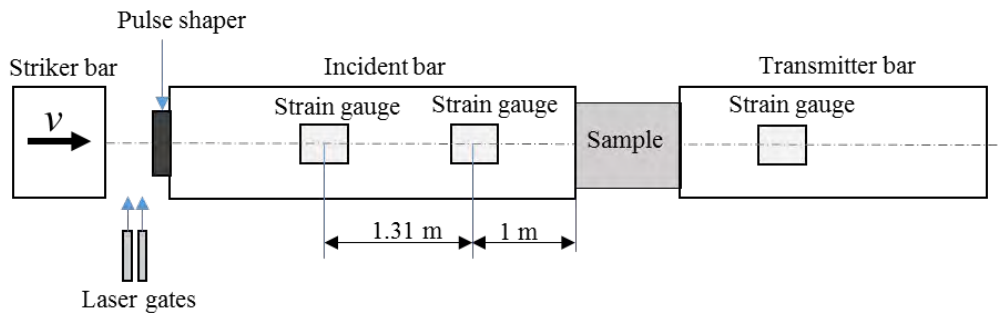
$$\epsilon_s(t) = -\frac{2c_b}{L_s} \int_0^t \epsilon_R(t) dt \quad (3)$$

$$\sigma_s(t) = \frac{A_b}{A_s} E_b \epsilon_T(t) \quad (4)$$

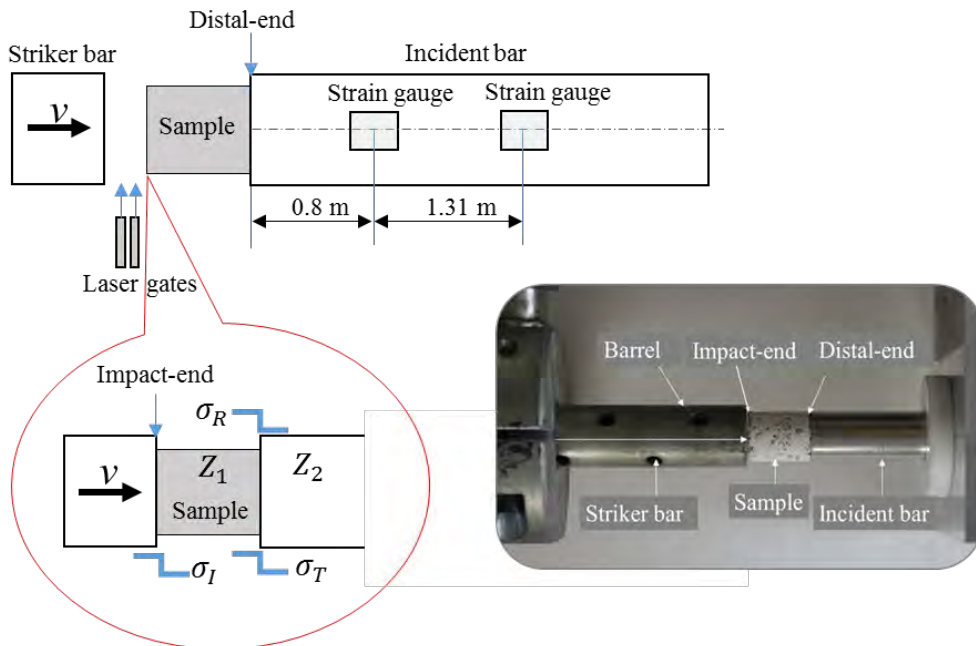
$$\dot{\epsilon}_s(t) = -\frac{2c_b}{L_s} \dot{\epsilon}_R(t) \quad (5)$$

where L_s , A_b , A_s , E_b , c_b and t are the length of sample, the cross-sectional area of bar and sample, elastic modulus and wave velocity of bar, and time, respectively. ϵ_R and ϵ_T are sequentially the reflected and transmitted strains.

Eqns. 3 through 5 are valid when the stress at the sample/incident bar interface is equal to the stress at the sample/transmitter bar interface [29, 33]. It was analytically shown by Davies and Hunter [29] that the stress equilibrium in SHPB is established when $T \geq \pi t_s$; where T is the duration of loading, t_s is the sample transit time (L_s / c_s) and c_s is the wave velocity of sample [29]. In other words, the incident stress wave should reverberate at least 3-4 times in the sample before the equilibrium is established [34]. In the SHPB testing of brittle materials, test sample may fracture within the initially steeply-rising part of incident stress wave at a time earlier than the time needed to establish the stress equilibrium (time to fracture $> \pi t_s$). In order to induce a gradually-rising incident wave, pulse shaping method is widely used [12]. In this method, a thin layer of a ductile metal is placed at the front of the incident bar so that the deformation of the thin-metal layer in between the striker and incident bar induces a gradually-rising stress wave on the incident bar. In the present study, an aluminum sheet in 10x10x2 mm size was used as a pulse shaper and placed at the front of the incident bar by applying a thin layer of lubricant. The tests satisfying the stress equilibrium in the SHPB are called “equilibrium tests” in the present study.



(a)



(b)

Figure 3. The schematic of (a) the SHPB compression test and (b) direct impact test together with the picture of the direct impact test

In the direct impact tests, the striker bar directly impinged on the test sample placed at the front of the incident bar with an initial velocity (v) as shown in Figure 3(b). The direct impact tests were performed at 10 m s^{-1} using a 500 mm-long Inconel striker bar and at 30 and 108 m s^{-1} using a 200 mm-long 1100 Al alloy striker bar. Higher velocities were attained using the lighter Al striker bar. In these tests, the distal-end stress (σ_D) shown in Figure 3(b) was calculated using the following relation

$$\sigma_D(t) = \frac{A_b E_b \varepsilon_i}{A_s} \quad (6)$$

where ε_i is the strain measured on the incident bar. Unlike the classical compression SHPB test, the distal-end stress is not equal to the impact-end stress in the direct impact test. Therefore, these are “non-equilibrium” tests. The calculation of the upper velocity for the stress equilibrium in the classical compression SHPB test is as follows. The strain in a long elastic bar is $\frac{v}{c}$; where v is the particle velocity and c is the elastic wave velocity. The quasi-static fracture strain (ε_f) of the tested AAC samples were determined around 0.02 and the elastic modulus $\sim 0.3 \text{ GPa}$.

By taking the density of ACC sample 600 kg m^{-3} , a particle velocity of $\sim 15 \text{ m s}^{-1}$ ($v = \varepsilon_f c$) was calculated at the fracture strain. Division this number by π gives an upper limit for the SHPB equilibrium test, $\sim 5 \text{ m s}^{-1}$. Above calculations should be taken as a rough estimate of the upper velocity limit as the fracture strain and elastic modulus of the tested sample may change with strain rate and the use of pulse shaper reduces the particle velocity of incident bar below that of striker bar. The lowest velocity used in the direct impact tests (10 m s^{-1}) is hence two times the calculated velocity for the stress equilibrium; therefore, the direct impact tests are considered as “non-equilibrium tests”. Note also that the impact-end stress could not be measured in the direct impact tests, while the strain was calculated indirectly by assuming a constant deformation velocity. For a constant deformation velocity, the sample should absorb only small portion of the kinetic energy of striker. The energy absorption of an AAC sample until fracture strain (~ 0.02) was calculated $\sim 0.9 \text{ J}$, while the energy of striker bar at 10, 30 and 108 m s^{-1} were ~ 61.6 , ~ 71.79 and $\sim 930 \text{ J}$, respectively. These calculations indicated that the maximum sample energy absorption was $\sim 1.5\%$ of that of the striker bar (10 m s^{-1}), confirming the constant deformation velocity assumption. The strain rates of non-equilibrium tests were calculated, based on the constant striker bar velocity, sequentially as ~ 385 , ~ 1150 and $\sim 4150 \text{ s}^{-1}$ for the tests at 10, 30 and 108 m s^{-1} .

In both classical SHPB compression and direct impact tests, the bar strains were measured some distance away from the sample/bar interfaces and were implemented in Eqns. 3 through 5 by assuming no wave-dispersion on the bars. In the used SHPB test apparatus, the strain gauges were 0.8 and 1 m away from the sample/bar interfaces for the direct impact and classical SHPB tests, respectively (Figures 3(a) and (b)). In order to account wave dispersion, two strain gauges (1.31 m apart) were mounted on the incident bar as seen in Figures 3(a) and (b). The strain readings from these two gauges were then used to check the wave-dispersion on the bars.

The impact of striker bar creates a compressive incident wave (σ_I) at the impact-end of the AAC sample as shown in Figure 3(b). This wave is reflected (σ_R) and transmitted (σ_T) at the distal end of the sample due to the mechanical impedance ($A\rho$, where A is the cross-sectional area and ρ is the density) difference between AAC sample and incident bar (Figure 3(b)). The ratio of the impedances of ACC sample/bar was calculated 90.2. The magnitudes of the reflected and transmitted waves from the distal-end are sequentially as

$$\sigma_R = \left(\frac{Z_2 - Z_1}{Z_1 + Z_2} \right) \sigma_1 \approx 0.02 \sigma_1 \quad (7)$$

$$\sigma_T = \left(\frac{2Z_2}{Z_1 + Z_2} \right) \left(\frac{A_1}{A_2} \right) \sigma_1 \approx 0.98\sigma_1 \quad (8)$$

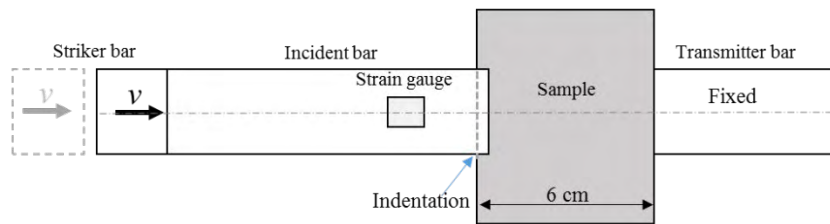
where Z_1 and Z_2 are the mechanical impedance of AAC sample and bar and A_1 and A_2 are the areas of AAC sample and bar, respectively. In the direct impact tests ($\geq 10 \text{ m s}^{-1}$), the wave created on AAC sample upon the impact of striker bar was transmitted to the incident bar by 98%. The wave was therefore assumed to be transmitted to the incident bar completely and the strain-gauge measured stresses on the incident bar nearly corresponded to the distal-end stress of ACC sample.

Quasi-static and high strain rate indentation and confined compression tests

The quasi-static indentation tests were conducted on 40x40x20 cm blocks using flat-ended 5, 10, 15, 20, 25 and 30 mm-diameter 304 steel indenters (Figure 4(a)) until about 25 mm depth of indentation at three different velocities, 5×10^{-5} , 5×10^{-4} , and $5 \times 10^{-3} \text{ m s}^{-1}$. The indenters were screwed to the Shimadzu Universal Testing Machine at the treated end, while 20 mm indenter was directly compressed on the blocks by the upper compression platen. The tested blocks were then cut into half at the mid-section of the indentation in order to observe the powder accumulation in the front of the indenter. The high strain rate indentation tests (10 m s^{-1}) were performed using a modified SHPB test. In these tests, AAC sample (6x6x6 cm) was inserted between the incident and transmitter bar (Figure 4(b)). The transmitter bar was tightened on its supports in such a way that during a test it did not move and the incident bar (19.4 mm in diameter) indented the sample. The difference between incident and reflected stresses gave the indentation dynamic strength of the tested sample.



(a)



(b)

Figure 4. The pictures of 5, 10, 15, 20, 25 and 30 mm indenters from left to right (a) and the schematic of dynamic indentation test (b)

A steel tube with an inner diameter of 19.35 mm, slightly smaller in diameter than the compression test sample, was used to perform the confined compression tests at quasi-static and high strain rates. The quasi-static tests were performed at $5 \times 10^{-4} \text{ m s}^{-1}$ and the dynamic tests at 8 m s^{-1} without using a pulse shaper. Before testing, the samples were inserted inside the steel tube with a wall thickness of 2 mm by applying a pressure. The schematics of the static and dynamic confined

compression tests are shown in Figures 5(a) and (b), respectively. In the quasi-static tests, the sample was compressed by a 100 mm-long Inconel bar which was just located under the loading plate. In dynamic tests, AAC sample was placed between the flat-ends of the incident and transmitted bar inside the confinement steel tube. Since the strength of the steel tube was much higher than that of AAC, the steel tube was assumed rigid.

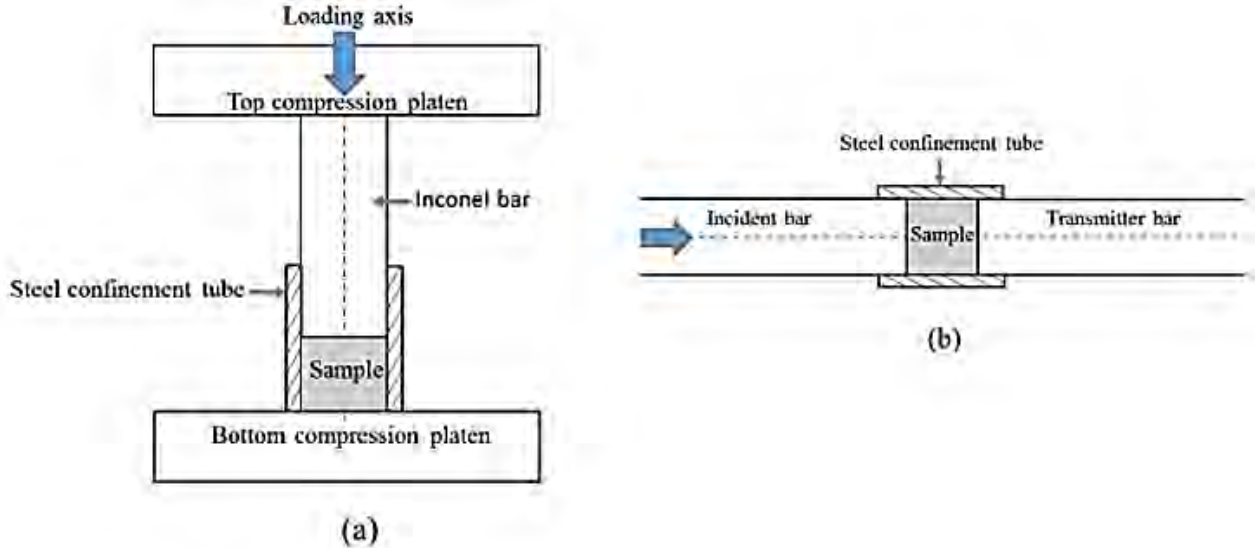


Figure 5. The schematics of confined compression tests (a) quasi-static and (b) high strain rate SHPB test

Results

Quasi-static and high strain rate compression tests

Typical incident and transmitter bar strain readings of the SHPB tests with and without pulse shaper at 8 m s^{-1} are shown in Figure 6(a). The time difference between the starting points of the reflected and transmitted waves is $\sim 25 \mu\text{s}$ (marked in Figure 6(a)) for both with and without pulse shaper tests and it is due to the wave transit time of the tested AAC sample. The use of pulse shaper as seen in the same figure increases the sample failure time from $45.5 \mu\text{s}$ to $100 \mu\text{s}$. An average elastic modulus of $\sim 0.75 \text{ GPa}$ was determined from the stress-strain curves at the same velocity. This corresponds to an elastic wave velocity of 1118 m s^{-1} and a transit time of $23 \mu\text{s}$ which is in accord with the measured transit time. The ratio of fracture time to transit time $\left(\frac{t_f}{t_t}\right)$ was calculated 1.82

and 4 for the tests with and without pulse shaper in Figure 6(a). Since the stress equilibrium was established only by using pulse shaper ($t_f \geq \pi t_t$), the SHPB compression tests were continued with the use of pulse shaper at 8 m s^{-1} (note that the velocity is lower on the incident bar). It is noted in Figure 6(a) that the front and back strain gauges mounted on the incident bar read almost the same strain, showing a negligible wave dispersion on the used Inconel 718 bars. Figure 6(b) shows the variation of stress and strain rate with strain in a typical SHPB test with a pulse shaper. As noted in the same figure, the strain rate varies with time until the fracture. The strain rate was then determined as the strain rate corresponding to the maximum stress. For the particular test shown in Figure 6(b); therefore, the strain rate at fracture is 185 s^{-1} . Note that after the failure, the strain rate increases as the sample becomes more compliant due to fracture. A common way of showing the stress equilibrium in the SHPB tests is to shift the waves to the sample/bar interface by a distance corresponding to the distance between sample and strain gauges and then calculate the equilibrium R value $\left(R = \frac{\sigma_1 + \sigma_R}{\sigma_T}\right)$. When this value reaches 1, the stress equilibrium is established in the sample.

As seen in Figure 6(b), the R value reaches 1 when the strain is ~ 0.007 . Figure 6(c) shows typical

strain gauge readings of the direct impact tests performed at 10 and 30 m s⁻¹. In these tests, front and back strain gauges were used to record the incoming wave after the impact of striker bar. The front and back gauge readings at 10 m s⁻¹ (using 50 mm-long Inconel bar) are almost the same, proving again an insignificant wave dispersion on the used Inconel bars. Also noted in the same figure that the time to fracture is 49 μs at 10 m s⁻¹, while it decreases to 34 μs at 30 m s⁻¹. These are non-equilibrium tests and prone to axial and radial inertia. The strain rates of non-equilibrium tests at 10, 30 and 108 m s⁻¹ striker bar velocities are sequentially ~385, ~1150 and ~4150 s⁻¹.

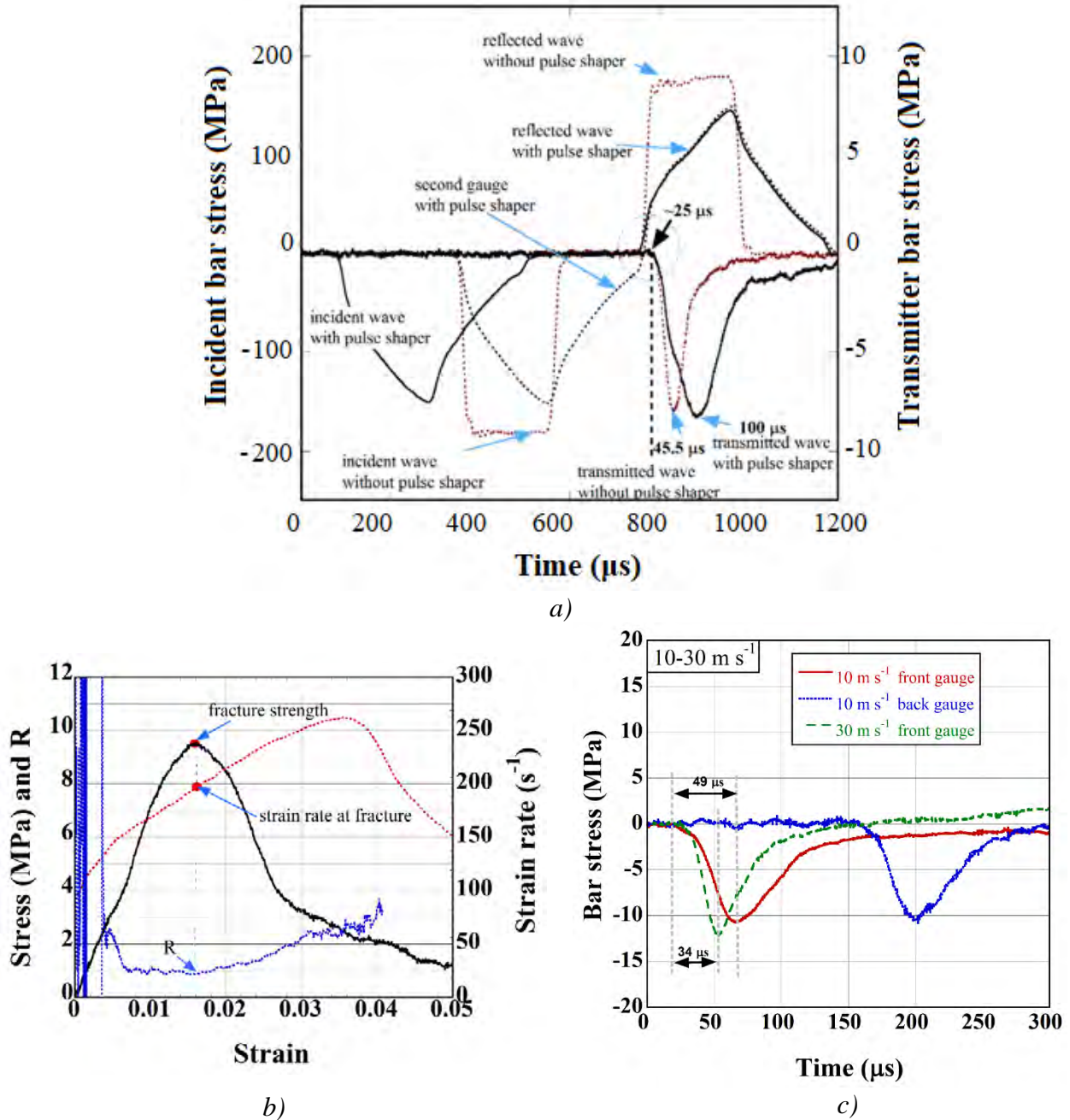


Figure 6. Typical SHPB incident and transmitter strain readings of the tests with and without pulse shaper (a) and typical stress-strain and strain rate-strain curve of SHPB test with pulse shaper (b) and direct impact test strain readings from front and back strain gauges at 10 and 30 m s⁻¹ (c)

The stress-strain curves of the quasi-static compression tests at 5x10⁻⁵ and the SHPB tests at 8 m s⁻¹ (using a pulse shaper, equilibrium test) are shown in Figures 7(a-b), respectively. The distal-end stress-time curves of the direct impact tests at 10, 30 and 108 m s⁻¹ are further shown in Figure

7(c). The maximum stress following the initial linear elastic region in these stress-strain curves is taken as the compressive strength (Figure 7(a)). As seen in Figures 7(a-c), the compressive strength increases as the velocity increases from quasi-static to 30 m s^{-1} , while the compressive strength slightly decreases when the direct impact velocity increases from 30 m s^{-1} to 108 m s^{-1} . The representative compression stress-strain curves of the tested AAC from $2 \times 10^{-3} \text{ s}^{-1}$ to 185 s^{-1} (8 m s^{-1} with pulse shaper) are shown in Figure 7(d). As noted in the same figure, the compression moduli at 35 and 185 s^{-1} are higher than those at the quasi-static strain rates, while the critical strains corresponding to the compressive strength are similar at different strain rates, $\sim 0.015\text{-}0.017$. At the highest strain rates, 1158 s^{-1} (30 ms^{-1}) and 4158 s^{-1} (108 ms^{-1}), the slopes of the initial linear region were however significantly reduced as compared with those of lower strain rates. The stress on the sample in the direct impact tests was measured only from the distal-end by the strain gauges mounted on the incident bar. Therefore, the stress measurement did not show the average stress of the sample at 1150 and 4150 s^{-1} as the axial and radial inertial effects were predominant at these strain rates. The mean compressive strengths of the tested AAC sample are listed in Table 1 together with test velocity, strain rate and the test type.

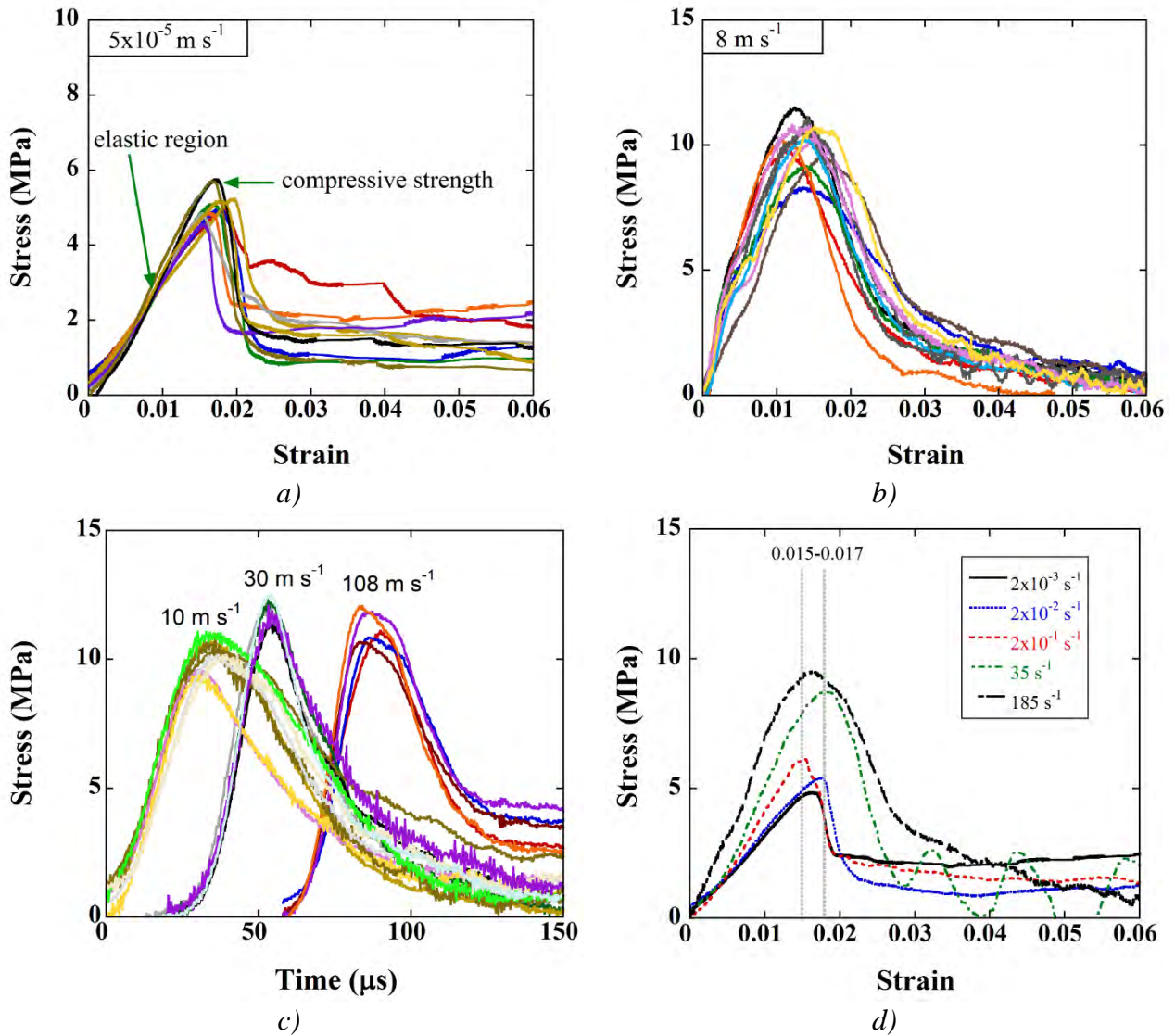


Figure 7. The compression stress-strain curves at (a) 5×10^{-5} and (b) 8 m s^{-1} (equilibrium test) and (c) the compression stress-time curves at 10 , 30 and 108 m s^{-1} and (d) the equilibrium test stress-strain curves at different strain rates

The failure at quasi-static velocities occurs by the initiation of a single axial crack at the bottom compression test platen as shown by arrows in Figures 8(a-b). Additional axial cracks, as seen in the same figures, then form as the upper compression test platen continuously compresses the sample. As opposite to quasi-static compression tests, the failure at increasing velocities from 1 to 108 m s⁻¹ starts from the impact-end (Figures 8(c-g)).

Table 1 The mean compression strengths of the quasi-static, drop-weight, SHPB and direct impact compression tests together with test velocity and strain rate and the type of test

Velocity (m s ⁻¹)	Approximate strain rate (s ⁻¹)	Test	σ_m (MPa)
5×10^{-5}	2×10^{-3}	Quasi-static compression	5.11
5×10^{-4}	2×10^{-2}	Quasi-static compression	5.37
5×10^{-3}	2×10^{-1}	Quasi-static compression	5.89
1	35	Drop-weight	7.34
8	185	SHPB	9.9
10	385	Direct impact	10.2
30	1150	Direct impact	11.70
108	4150	Direct impact	11.60

The failure at quasi-static velocities occurs by the initiation of a single axial crack at the bottom compression test platen as shown by arrows in Figures 8(a-b). Additional axial cracks, as seen in the same figures, then form as the upper compression test platen continuously compresses the sample. As opposite to quasi-static compression tests, the failure at increasing velocities from 1 to 108 m s⁻¹ starts from the impact-end (Figures 8(c-g)).

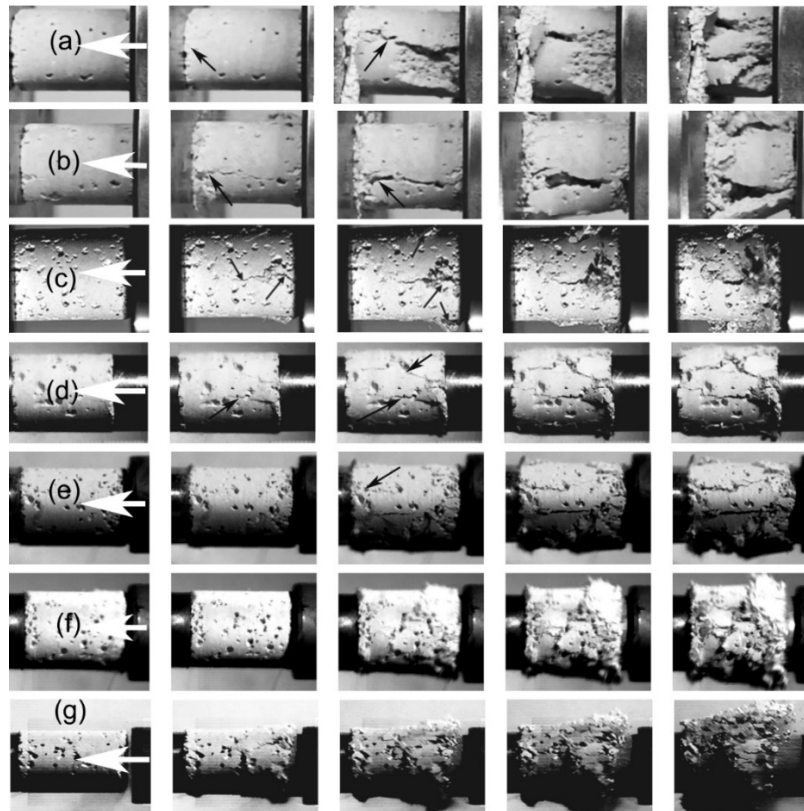


Figure 8. The deformation pictures of the samples tested at (a) 5×10^{-5} , (b) 5×10^{-3} (c) 1 (drop tower), (d) 8 (SHPB), (e) 10 (f) 30 and (g) 108 m s⁻¹ at different displacements before and after the failure (the white arrows show the upper compression test platen in quasi-static tests and the impact-end in dynamic tests and the black ones show the cracks)

The failure in drop-weight test and at 8 and 10 m s⁻¹ also occurs dominantly by axial cracking, while circumferential cracks at the impact-end are also noted (Figures 8(c-e)). However, the extensive cracking composing of both axial and circumferential cracks is seen at the impact-end of the samples tested at 30 and 108 m s⁻¹ (Figures 8(f) and (g)). The number of cracks also increase significantly at these velocities, clearly indicating the effect of velocity on the fracture behavior of the tested AAC.

Quasi-static and dynamic indentation and confined compression tests

Figure 9(a) shows the indentation force-displacement curves of 5 and 10 mm indenters at 5x10⁻⁵ m s⁻¹. A mean force of 5 tests for each indenter was calculated as seen in the same figure. The indentation force initially increases linearly with increasing displacement until about a critical force at which the indenter starts to penetrate the sample. Following the indenter penetration, the force increases less gradually with increasing displacement. As seen in Figure 9(b), the average indentation stress (mean force/indenter area) decreases as the indenter size increases, while the indentation stress saturates at and above 25 mm indenter sizes. The increase of indentation stress with increasing displacement is partly due to the powder accumulation in the front of indenter as depicted in the inset of Figure 9(b) for 30 mm indenter. Figure 9(c) shows the indentation stress-displacement curves of 20 mm indenter at 5x10⁻⁵, 5x10⁻⁴ and 5x10⁻³ m s⁻¹.

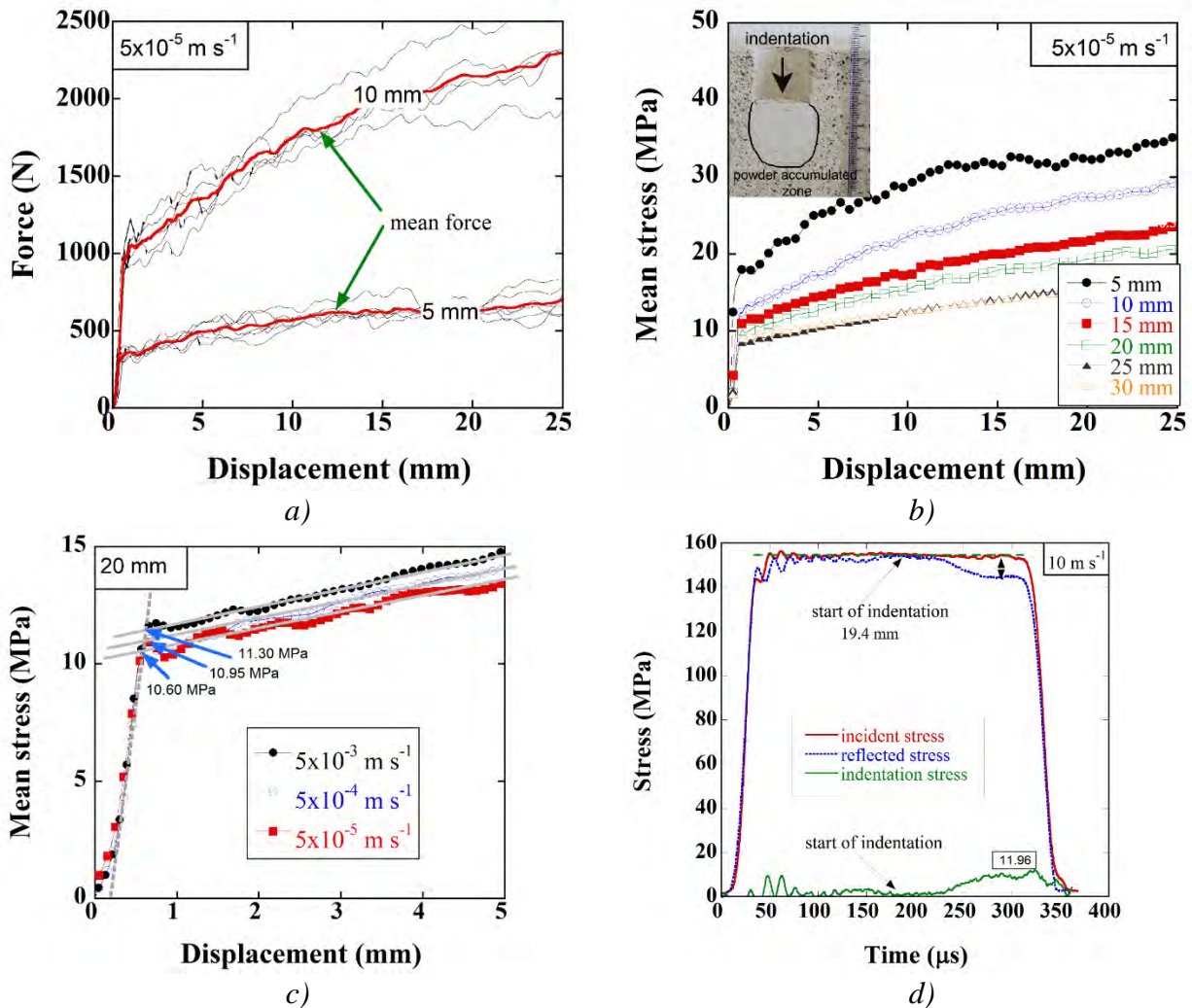


Figure 9. the indentation force-displacement and mean force-displacement curves of 5 and 10 mm indenters at 5x10⁻⁵ m s⁻¹ (a), mean stress-displacement curves at different indenter sizes at 5x10⁻⁵ m s⁻¹ (b), indentation stress-displacement curves using 20 indenter at different velocities and determination of indentation strength (c) and the stress-time curve of a dynamic indentation test using 19.4 mm incident bar (d)

As shown in the same figure, the intercept of a linear line drawn in the elastic region and a linear line drawn in the indenter penetration region is taken as the average indentation strength which corresponds to the stress at which the indenter starts to penetrate the sample. In the calculations of the indentation strength, the shear and frictional forces were not taken into account. However, the saturation of the indentation strength after 25 mm indenter size implies that the compression force is significantly higher than the shear and frictional forces and therefore can be used to calculate the indentation strength. Figure 9(d) shows the incident and reflected (shifted) stresses of a SHPB indentation test together with the calculated indentation stress at 10 m s^{-1} . The indentation stress was calculated as the stress difference between incident and shifted-reflected stresses. As noted in the same figure, the indentation of the incident bar to the sample starts after about a time which is reflected as the reduced reflected stress in Figure 9(d). The indentation stresses were calculated 11.96, 11.54 and 12.10 MPa with an average of 11.87 MPa at 10 m s^{-1} .

No pulse shaper was used in the confined compression tests since the samples in these tests deformed without fracture until about large strains. Typical SHPB test incident, reflected and transmitted waves of the confined compression test at 8 m s^{-1} are shown in Figure 10(a). The strain rate in these tests was almost constant and approximately 330 s^{-1} . As noted in the same figure, the time difference between starting points of the reflected and transmitted waves is again $\sim 25 \mu\text{s}$ and the confinement tube is not relaxed quickly, imposing a residual stress on the transmitter bar at the end of the transmitter bar strain reading (Figure 10(a)). Figure 10(b) shows the stress-strain curves of the confined compression tests at $5 \times 10^{-4} \text{ m s}^{-1}$ and 8 m s^{-1} . The confined tests at quasi-static strain rate continued until about large strains (0.4) and the sample was compressed (densified) without fracture as depicted in the inset of Figure 10(b). The initial linear elastic region of the confined tests in Figure 10(b) is followed by a non-linear increase of the stress after about a strain of 0.02. The corresponding stress at 0.02 strain is taken as the confinement strength and it varies between 4.83 and 8.51 MPa ($\sigma_m = 7.73 \text{ MPa}$). These values are higher than the fracture strengths of the unconfined tests at the same velocity ($\sigma_m = 5.89 \text{ MPa}$). The samples tested at 8 m s^{-1} are again densified as the strain increases and show almost no fracture as depicted in the inset of Figure 10(b). The final strain attained in these tests is about 6%.

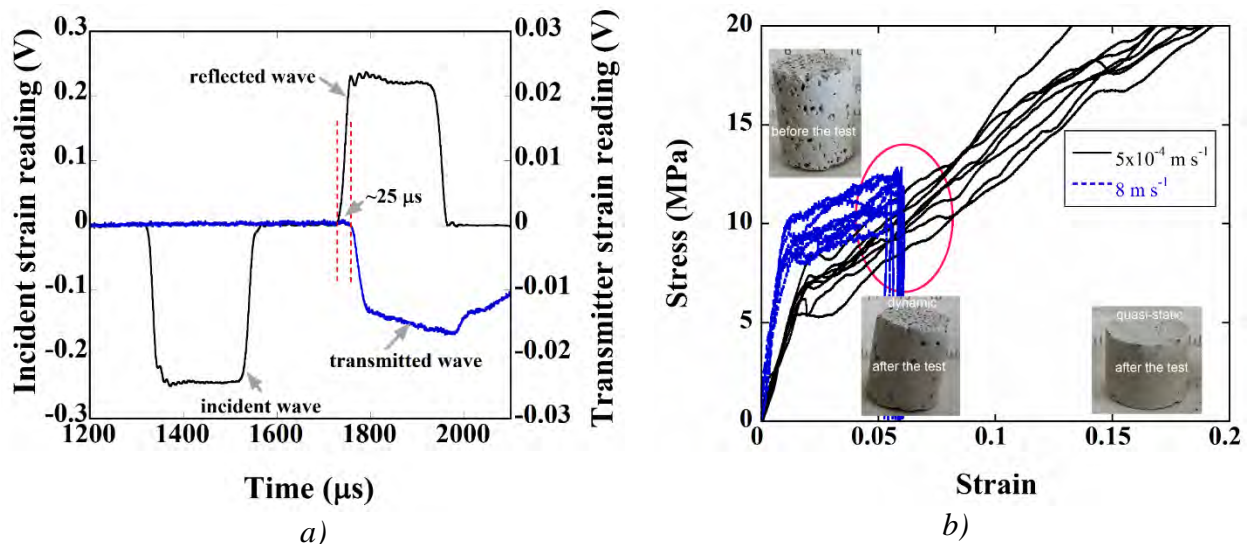


Figure 10 (a) the incident and transmitter strain readings of a confined compression test in SHPB at 8 m s^{-1} and (b) the dynamic and static confined compression stress-strain curves and the pictures of deformed and recovered test samples

The compressive strengths of confined SHPB tests are however slightly lower than those of unconfined SHPB tests, varying between 7.96 and 10.42 MPa with a mean stress of 9.11 MPa at $\sim 330 \text{ s}^{-1}$ (the mean strength of unconfined compression tests is 9.85 MPa at 185 s^{-1}). The confined

compression strengths of SHPB tests are however higher than of those of quasi-static tests as shown in Figure 10(b). Although the dynamic confined compression tests show higher initial stresses, the stresses of both tests approach to each other at increasing strains as seen in Figure 10(b).

Discussion

The variations of the compression (Table 1) and confined compression and compression and mean indentation (20 and 30 mm) strengths are shown in Figures 11(a) and (b), respectively. Note that as the stresses on the sample was measured only from the distal-end by the strain gauges mounted on the incident bar in the direct impact tests, the stress measurement did not show the average stress of the samples tested at 320, 1150 and 4150 s⁻¹. The compressive strength variation in Figure 11(a) may be considered in two sequential regions: a lower velocity-dependent strength region (Region 1-solid line) at quasi-static velocities and a higher velocity-dependent strength region (Region 2-dashed line) at high velocities, showing the first turning point of the s-type curve.

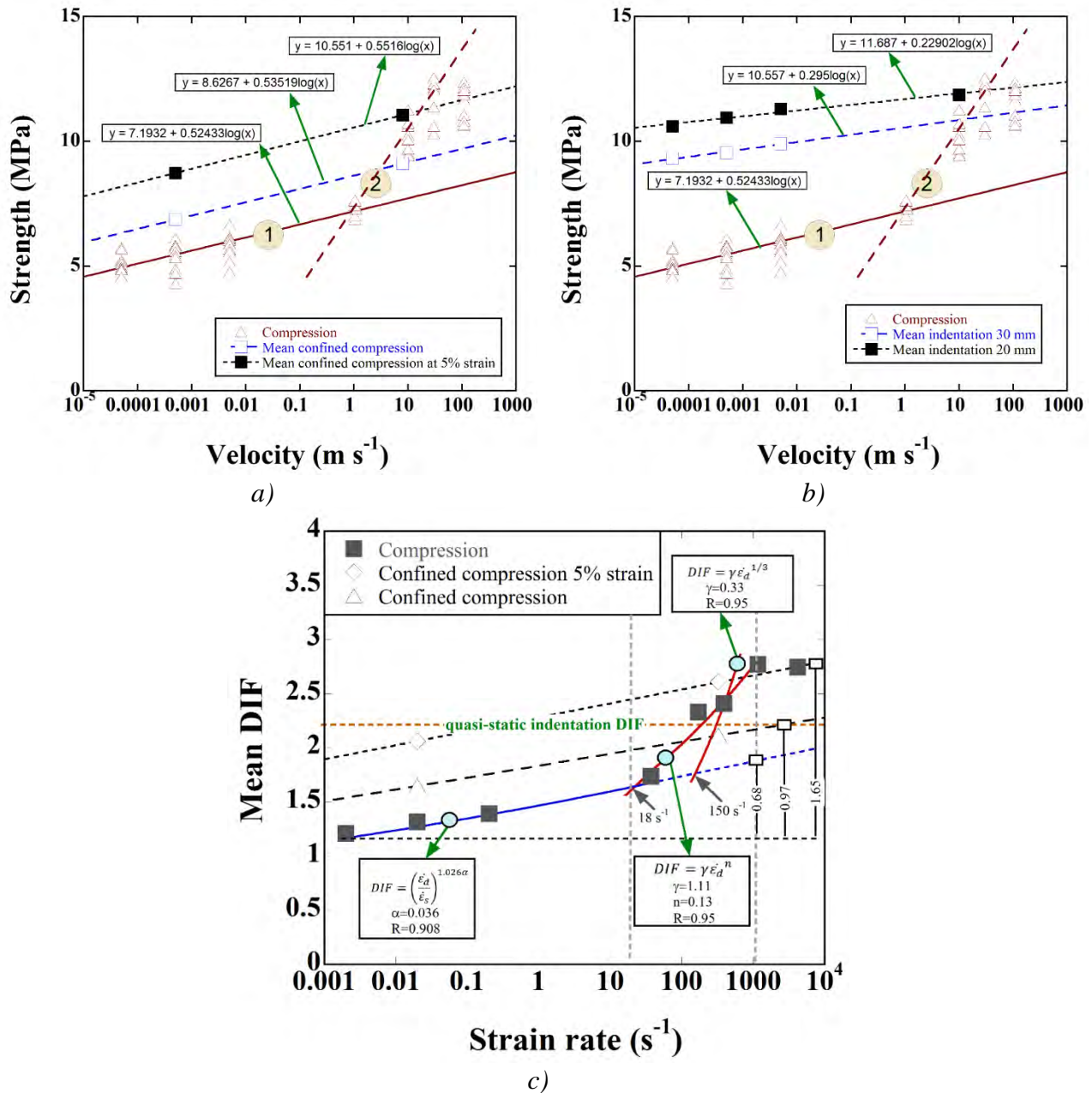


Figure 11. The variations of strength with velocity in (a) compression and confined compression tests and (b) compression and indentation tests, and (c) the mean DIF values as function of strain rate

The confined compression stresses at 5% strain are also shown in the same figure for comparison. One of the problems in the dynamic and quasi-static confined compression tests is the establishment of a full-confinement state since the material near the confinement-circular-steel-tube-wall fractures easily, resulting in reduced pressure on the sample and hence invalidating a full-confinement state. The second problem is the prevention of the friction forces between sample and confinement-tube wall. Third, increasing strain also increases confinement stress. Nevertheless, the mean confined and indentation strength values in the same figure increase as the velocity increases. The mean indentation strength values, showing presumably the full-confined state, are slightly higher than the mean confined compression strength values (Figure 11(b)). The dynamic indentation tests using the incident bar (19.4 mm) also result in similar mean strength values with the dynamic compression tests. The results of linear fits to the compression, mean indentation and confined compression strength values are also shown in Figures 11(a) and (b). The fitting results show comparable slopes between the confined compression and compressive strength, while the slope of the indentation strength is lower than that of the compressive strength in Region 1.

The failure of brittle materials proceeds with crack opening and growth. At quasi-static strain rates, the energy needed for crack opening is much higher than the energy needed for crack growth. Therefore, few cracks grow under static loading through the weakest path along in the axial direction. At increasing strain rates, there is however less time for both crack opening and growth. This causes an increase in the strength and number of micro cracks formed at increasing strain rates. The fracture mechanism considered here is thermally activated and both increasing strain rate and decreasing temperature increase the fracture strength of concrete [17-19]. A similar effect was also found in the present study. Until about 8 m s^{-1} , the main failure mechanism was the axial crack formation and propagation, while circumferential cracks developed at and after 30 m s^{-1} . The specimen pulverizations at the impact-end after a critical velocity seen in Figures 8(e) and (d) also agreed with a previous study on AAC sample [11].

Furthermore, the cracks were observed to initiate at the impact-end and then propagated axially normal to the circumferential tensile strain (Poisson's expansion) at low strain rates. At increasing strain rates, the cracks propagated normal to the axial loading direction (circumferential cracks). As the radial inertia became more effective at increasing strain rates, the increased constraint effect induced a complex deformation pattern accompanied with the stress wave reflections from the already formed-crack surfaces, the cell walls and edges and also from the surfaces of the sample. The crack bifurcation presumably resulted in fragmentation at the impact-end. The International Federation for Structural Concrete (CEB) recommended two empirical equations to define the DIF of concrete strength as [35]

$$DIF = \frac{\sigma_d}{\sigma_s} = \left(\frac{\dot{\epsilon}_d}{\dot{\epsilon}_s} \right)^{1.026\alpha} \quad \dot{\epsilon}_d \leq 30s^{-1} \quad (9)$$

$$DIF = \frac{\sigma_d}{\sigma_s} = \gamma \dot{\epsilon}_d^{1/3} \quad \dot{\epsilon}_d > 30s^{-1} \quad (10)$$

where, $\dot{\epsilon}_d$ and $\dot{\epsilon}_s$ are the dynamic and static strain rates. The value of $\dot{\epsilon}_s$ is $3 \times 10^{-5} \text{ s}^{-1}$, $\gamma = 10^{6.156-2}$ and $\alpha = \frac{1}{\left(5 + \frac{\sigma_s}{10}\right)}$. Figure 11(c) shows the mean DIF values of the compressive strength as function

of strain rate and the fitting parameters of Eqn. 9 and Eqn. 10. The value of α in Eqn.9 and γ in Eqn. 10 is ~ 0.036 and ~ 0.33 , respectively. The critical strain rate for the increased compressive strength

is predicted 150 s^{-1} in Figure 11(c). The dynamic compressive strength values are also fitted with $\frac{\sigma_d}{\sigma_s} = \gamma \dot{\epsilon}_d^n$, where $n=0.13$ and $\gamma=1.11$, which results in a critical strain rate of $\sim 18 \text{ s}^{-1}$ as shown in

Figure 11(c). This equation shows a better fit to the DIF than Eqn. 10. Since the strain rate in indentation tests cannot be determined, the mean DIF value of the quasi-static indentation tests is shown as a dotted line in Figure 11(c). Assuming a full confinement state in the indentation tests, an increase of 0.97 in the DIF is found between 2×10^{-3} and 1150 s^{-1} (Figure 11(c)). The extrapolation of the Eqn. 9 to 1150 s^{-1} in the same strain rate interval gives an increase of 0.68 in the DIF. The addition of both values (0.97 and 0.68) results in an increase of 1.65 in the DIF between 2×10^{-3} and 1150 s^{-1} , which is the same as the experimentally determined increase in the DIF (1.65) in the same strain rate interval as shown in Figure 11(c). From these results, the inertia and strain rate contributions to the enhancement of DIF until 1150 s^{-1} are determined about 60% and 40%, respectively. Linear fits to mean DIF values of confined compression strengths also give the similar slopes with that of the compressive strength in Region 1 as shown in Figure 11(c).

The critical strain rate for the passage to the 1D state of strain was shown to depend on the diameters of test samples; larger diameters showed larger inertial effects; hence, lower critical strain rates for the passage to the 1D state of strain [28]. The strength values measured in the present study correspond to non-equilibrium tests at and above 10 m s^{-1} . Therefore, the strength values above this velocity corresponded to the distal-end stress in the SHPB, while the impact-end stress might be larger and can only be determined through the finite element simulations or measured by placing impedance-matched quartz crystals at the impact-end of tested sample. This is left for future studies. Also, the calculated contributions of strain rate and inertia to the strength should be carefully approached as these ratios are both geometry and material dependent, hence cannot be generalized.

When modelling such brittle cellular materials against impact loading, the inertial effects should be excluded from constitutive equation. In many occasions, the stress rise due to inertia is considered as the material's intrinsic response to increasing strain rates, an effect which is also seen in testing ceramic materials. The results of this study emphasize this fact, besides following a scientific curiosity on the strain rate sensitivity of brittle cellular structures.

Conclusions

The strain rate dependent compressive strength of an autoclaved aerated concrete with a density of 600 kg m^{-3} was experimentally investigated between quasi-static ($2 \times 10^{-3} \text{ s}^{-1}$) and dynamic ($\sim 4150 \text{ s}^{-1}$) strain rates. High strain rate equilibrium and direct impact non-equilibrium compression tests were conducted in a compression Split Hopkinson Pressure Bar. Quasi-static and high strain rate indentation and confinement compression tests were also implemented in order to clarify the effect of confinement on the fracture strength. The experimental results showed two different regions of compressive strength-dependency on the strain rate: a low-strain rate-dependent region from quasi-static to $\sim 18 \text{ s}^{-1}$ and a high-strain-rate dependent region from $\sim 18 \text{ s}^{-1}$ to higher strain rates. In parallel with this, the failure at quasi-static velocities occurred by the progression of a single axial crack initiated at the bottom compression test plate. At increasing velocities; however, the extensive cracking of the sample composing of both axial and circumferential cracks was detected, showing the effect of inertia on the fracture behavior of the tested autoclaved aerated concrete. The mean confined and indentation strength values also increased as the velocity increased and the mean confined compression strength values were shown comparable with the dynamic compressive strength values in the low-strain rate-dependent region. The contributions of the inertia and strain rate to the enhancement of dynamic increase factor until about 1000 s^{-1} were predicted about 60% and 40% for the studied test sample and its geometry, respectively.

Acknowledgement

Authors would like to thank AKG Gaz Beton of Turkey for providing AAC blocks for the present study.

The authors declare that they have no conflict of interest.

REFERENCES

- [1] Narayanan, N., Ramamurthy, K. *Structure and properties of aerated concrete: a review*. Cement and Concrete composites, 2000, 22, pp. 321-329.
- [2] Scheffler, M., and Colombo, P. *Cellular ceramics*. Structure, Manufacturing, Properties and Applications, 2005, 670 p.
- [3] Hu W., Neufeld, R.D., Vallejo, L.E., Kelly, C. and Latona, M. *Properties of autoclaved cellular concrete with high volume fly ash*. J Energy Eng-ASCE, 1997, 123, pp 44-54.
- [4] Narayanan, N. and Ramamurthy, K. *Microstructural investigations on aerated concrete*. Cement and Concrete Research, 2000, 30, pp. 457-464.
- [5] Ramamurthy, K. and Narayanan, N. *Influence of composition and curing on drying shrinkage of aerated concrete*. Materials and Structures, 2000, 33, pp. 243-250.
- [6] Bonakdar, A., Babbitt, F. and Mobasher, B. *Physical and mechanical characterization of Fiber-Reinforced Aerated Concrete (FRAC)*. Cem Concr Compos, 2013, 38, pp. 82-91.
- [7] Chen, Y., Peng, M., Zhang, Y. and Liu, Y. *Mechanical Properties of Autoclaved Aerated Concrete with Different Densities*, 2013.
- [8] Fapohunda, C., Ikponmwosa, E. and Falade, F. *Evaluation of strength relations in foamed aerated concrete containing pulverized bone (PB) as a partial replacement of cement*. Engineering Review, 2018, 38, pp. 20-29.
- [9] Yankelevsky, D.Z. and Avnon, I. *Autoclaved aerated concrete behavior under explosive action*. Construction and Building Materials, 1998, 12, 359-364.
- [10] Mespoulet, J., Plassard, F. and Hereil, P.L. *Strain rate sensitivity of autoclaved aerated concrete from quasi-static regime to shock loading*. In: Dymat 2015 - 11th International Conference on the Mechanical and Physical Behaviour of Materials under Dynamic Loading, E. Cadoni (Ed). E D P Sciences, Cedex A.
- [11] Belouettar, R., Klepaczko, J.R. and Edps. *A study of dynamic behavior of the autoclaved aerated concrete*. DYMAT 2009 - 9th International Conference on the Mechanical and Physical Behaviour of Materials under Dynamic Loading, 2009, Vol. 1, pp. 503-509.
- [12] Khosravani, M.R. and Weinberg, K. *A review on split Hopkinson bar experiments on the dynamic characterisation of concrete*. Constr Build Mater, 2018, 190, pp. 1264-1283.
- [13] Brace, W.F. and Jones, A.H. *Comparison of uniaxial deformation in shock and static loading of 3 rocks*. Journal of Geophysical Research, 1971, 76, pp. 4913-4921.
- [14] Grady, D.E. *Shock-wave compression of brittle solids*. Mechanics of Materials, 1998, 29, pp. 181-203.
- [15] Yu, S.S., Lu, Y.B. and Cai, Y. *The strain-rate effect of engineering materials and its unified model*. Lat Am J Solids Struct, 2013, 10, pp. 833-844.
- [16] Bischoff, P.H. and Perry, S.H. *Compressive behavior of concrete at high-strain rates*. Materials and Structures, 1991, 24, pp. 425-450.
- [17] Zhang, Q.B. and Zhao, J. *A Review of Dynamic Experimental Techniques and Mechanical Behaviour of Rock Materials*. Rock Mech Rock Eng, 2014, 47, pp. 1411-1478.
- [18] Lu, D.C., Wang, G.S., Du, X.L. and Wang, Y. *A nonlinear dynamic uniaxial strength criterion that considers the ultimate dynamic strength of concrete*. International Journal of Impact Engineering, 2017, 103, pp. 124-137.
- [19] Lindholm, U.S., Yeakley, L.M. and Nagy, A. *The dynamic strength and fracture properties of dresser basalt*. International Journal of Rock Mechanics and Mining Sciences & Geomechanics Abstracts, 1974, 11, pp. 181-191.
- [20] Reinhardt, H.W., Rossi, P., van Mier. *Joint investigation of concrete at high rates of loading*. Structures, 1990, 23, pp. 213-216.
- [21] Wang, Q.F., Liu, Y.H. and Peng, G. *Effect of water pressure on mechanical behavior of concrete under dynamic compression state*. Construction and Building Materials, 2016, 125, pp. 501-509.

- [22] Rossi, P.J.M. and Structures. *A physical phenomenon which can explain the mechanical behaviour of concrete under high strain rates*. 1991, 24, pp. 422-424.
- [23] Rossi, P., Toutlemonde F.J.M. and Structures. *Effect of loading rate on the tensile behaviour of concrete: description of the physical mechanisms*. 1996, 29, 116 p.
- [24] Zeng, S.J., Ren, X.D. and Li, J. *Triaxial Behavior of Concrete Subjected to Dynamic Compression*. J Struct Eng-ASCE, 2013, 139, pp. 1582-1592.
- [25] Legeron, F. and Paultre, P. *Uniaxial confinement model for normal- and high-strength concrete columns*. J Struct Eng-ASCE, 2003, 129, pp. 241-252.
- [26] Sfer, D., Carol, I., Gettu, R. and Etse, G. *Study of the behavior of concrete under triaxial compression*. J Eng Mech-ASCE, 2002, 128, pp. 156-163.
- [27] Lahlou, K., Lachemi, M. and Aitcin, P.C. *Confined high-strength concrete under dynamic compressive loading*. J Struct Eng-ASCE, 1999, 125, pp. 1100-1108.
- [28] Liu, F. and Li, Q.M. *Strain-rate effect on the compressive strength of brittle materials and its implementation into material strength model*. International Journal of Impact Engineering, 2019, 130, pp. 113-123.
- [29] Davies, E.D.H. and Hunter, S.C. *The dynamic compression testing of solids by the method of the split Hopkinson pressure bar*. Journal of the Mechanics and Physics of Solids, 1963, 11, pp. 155-179.
- [30] Tekoglu, C., Gibson, L.J., Pardoen, T. and Onck, P.R. *Size effects in foams: Experiments and modeling*. Progress in Materials Science, 2011, 56, pp. 109-138.
- [31] Jin, T., Zhou, Z.W., Wang, Z.H., Wu, G.Y. and Shu, X.F. *Experimental study on the effects of specimen in-plane size on the mechanical behavior of aluminum hexagonal honeycombs*. Mater Sci Eng A-Struct Mater Prop Microstruct Process, 2015, 635, pp. 23-35.
- [32] ASTM C. *Standard test method for compressive strength of cylindrical concrete specimens*. In: Book Standard test method for compressive strength of cylindrical concrete specimens, 2019.
- [33] Kolsky, H. *An Investigation of the Mechanical Properties of Materials at Very High Rates of Loading*. Proceedings of the Physical Society Section B, 1949, 62(11), pp. 676-700.
- [34] Ravichandran, G. and Subhash, G. *Critical-appraisal of limiting strain rates for compression testing of ceramics in a split hopkinson pressure bar*. J Am Ceram Soc, 1994, 77, pp. 263-267.
- [35] CEB. *Concrete structures under impact and impulsive loading*. In: Book Concrete structures under impact and impulsive loading. Bulletin d'information, 1998, No 187, CEB Comite' EuroInternational du Be'ton.

Received: 28.01.2023

Accepted: 15.05.2023